Supplementary Information (SI) for ChemComm.
This journal is © The Royal Society of Chemistry 2024

Supporting Material

Unveiling the effect of codoping in strontium ferrite for oxygen evolution in alkaline media

Shuangshuang Zhu,[a,†] Mingyuan Wang,[b,†] Yuguang Mao,[a] Jiayuan Wang,[a] Jiabao Ding,[a,*] Guiwu Liu[c] and Weifeng Zhang[a,d,*]

[a]Henan Key Laboratory of Quantum Materials and Quantum Energy, School of Future Quantum Information Technology, Henan University, Zhengzhou 450046, China.

[b]School of Mechanical Engineering, Jiangsu University, Zhenjiang, 212013, China.

[c]School of Materials Science and Engineering, Jiangsu University, Zhenjiang 212013, China.

[d]Institute of Quantum Materials and Physics, Henan Academy of Sciences, Zhengzhou 450046, China.

[*]To whom correspondence should be addressed. E-mail: jbding@henu.edu.cn; wfzhang@henu.edu.cn

[†]These authors contribute equally.

Experimental Section

Chemicals

$SrCO_3$(99.99%) was purchased from Tianjin Guangfu Fine Chemical Research Institute. Fe_2O_3 (99.90%), NiO (99.99%), and Co_2O_3 (99.99%) were purchased from Shandong West Asia Chemical Industry Co., Ltd. KOH (99.99%), Nafion (5%wt) and C_3H_8O (≥99.7%) were purchased from Sigma-Aldrich.

Synthesis of perovskite oxides

The perovskite oxides were synthesized by a solid-state method. To prepare Co and Ni codoped strontium ferrite, stoichiometric amounts of $SrCO_3$, Fe_2O_3, NiO, and Co_2O_3 were mixed in a mortar and thoroughly ground for 2 h. The mixture was dried in an oven at 343 k overnight, calcined at

1273 K in a box furnace for 12 h, and then cooled to 573 K with rate of 4 k min^{-1}, which was then cooled naturally to room temperature.

Characterization

Powder X-ray diffraction (XRD) patterns were collected on a Bruker D8 Advance X-ray diffractometer with a Cu Kα radiation source (λ = 1.5418 Å). The transmission electron microscope (TEM) images and high-resolution transmission electron microscopy (HRTEM) images were obtained with a JEM-F200 microscope equipped with a field emission gun operating at 200 kV. The high-angle annular dark-field scanning transmission electron microscope (HAADF-STEM) and EDS elemental mapping were recorded on the FEI Titan Themis apparatus with an X-FEG electron gun and a DCOR aberration corrector operating at 300 kV. Scanning electron microscopy (SEM) images were studied on a JSM 7001F electron microscope at 10 kV. Energy dispersive X-ray analysis (EDS) was obtained by SEM was performed using the EDS system on JSM-7610F. X-ray photoelectron spectroscopy (XPS) was performed on thermo Fischer, ESCALAB Xi+ spectrometer. The contents of the metals were determined by inductively coupled plasma atomic emission spectroscopy (ICP-AES, 7800, Agilent).

Electrochemical measurements

The electrochemical measurements were carried out in a three-electrode system containing 1 M KOH with the glassy carbon electrode (GCE, 5 mm in diameter) as the working electrode. The Hg/HgO was the reference electrode (1 M KOH) and the carbon rod was the counter electrode. To prepare the catalyst ink, the catalyst (10 mg) was mixed with carbon VXC-72, 5 mg) in isopropanol by sonication and then centrifuged to obtain the powder. The powder was dried in an oven overnight.

The dried powder (4 mg), isopropanol (370 μL), and 5 wt% Nafion solution (30 μL) were ultrasonicated to prepare the ink, and 70 μL of the ink was dropped onto the GCE surface to prepare the working electrode. The polarization curves were recorded at a scanning at a scanning rate of 5 mV s^{-1} with 85% iR-drop compensation. Electrochemical impedance spectroscopy EIS measurements are performed at 0.65 V (vs. Hg/HgO) with frequencies ranging from 100 kHz to 0.1 Hz. The durabilities of the samples were studied by comparing the LSV change before and after a given number of consecutive CV scans (scan rate 100 mV s^{-1}) and chronopotentiometric measurements. The chronopotentiometric measurements were carried out at a current density of 10 mA cm^{-2} without iR-correction with 70 μL of the ink dropped onto the GCE. To conveniently characterize the structure of the sample after a durable test, the ink was dropped onto carbon paper (0.25 cm^2) with the same catalyst loading on GCE.

The potential of the reference electrode was calibrated to reversible hydrogen electrode (RHE) by the following method: First, two Pt electrodes that act as working electrode and counter electrode were cleaned by cycling in 1 M H_2SO_4 between -2 and 2 V for 2 h and washed with water. Before the calibration, the electrolyte (1 M KOH) was saturated with H_2 by continuously bubbling H_2 for half an hour. During the calibration, hydrogen was bubbled over the working electrode. A series of controlled-potential chronoamperometric curves were measured for 300 s to get the current between the hydrogen oxidation and hydrogen evolution. The resulting potential is the potential of zero net current. In this work, the potential of zero net current was found at -0.940 V versus the Hg/HgO electrode in 1 M KOH (Fig. S7). Thus, the potentials, measured against Hg/HgO, were converted into the potentials versus RHE by using the equation as follows:

$$E(RHE) = E(Hg/HgO) + 0.940\ V \quad (1)$$

To calculate the effective electrochemical active surface area (ECSA), the CV curves were measured in a non-faradaic potential range at the scan rates of 10, 20, 40, 60, 80, and 100 mV s^{-1}. The geometric double layer capacitance (C_{dl}) was obtained by plotting the difference of current density ΔJ = (Janodic − Jcathodic) / 2 at 1.15 V vs. RHE against the scan rates, and the slope of the linear trend was C_{dl}. The ECSA was estimated according to the equation:

$$ECSA = C_{dl} / Cs \quad (2)$$

Where the Cs is estimated to be 0.06 mF cm^{-2}. The TOF values of samples were calculated based on the number of active sites using the following equation:

$$TOF = J*A / (4*F*n) \quad (3)$$

Where j and A are the current density (A cm^{-2}) and the area of the electrode (0.196 cm^2). F is the Faraday constant (96485 C mol^{-1}) and n is the molar number of metallic atoms at the B-site in a perovskite oxide that dropped on the electrode.

Computational method

In this work, the calculations were performed by density functional theory (DFT) based on the Vienna Ab initio Simulation Package (VASP).[1] The GGA and PBE functions were applied to describe the exchange-correlation function.[2] The ion-electron interaction is described by using the projector augmented wave (PAW) method.[3] A vacuum space of at least 15 Å was included in the unit cell to minimize the interactions

between the system and its replicas resulting from the periodic boundary condition.[4,5]. A cut-off energy of 400 eV was set and the Brillouin Zone was chosen as 3×3×1 grid, and the convergence criteria of energy and force were set as 10^{-4} eV per atom and 0.02 eV/Å, respectively.[6]

The standard hydrogen electrode model is adopted to calculate the Gibbs free energy[7]:

$$\Delta G = \Delta E + \Delta E_{ZPE} - T\Delta S$$

Where ΔE, ΔE_{ZPE}, and ΔS are the adsorption energy, changes in zero-point energy and entropy, respectively. ΔE_{ZPE} and ΔS are calculated by vibration frequency. T is temperature (298.15 K). The ΔE, ΔE_{ZPE}, and ΔS were calculated through the equation:

$$\Delta E = \Delta E_{total} - E_{surface} - E_{gas} \quad (5)$$

$$E_{ZPE} = \frac{1}{2}\sum_i h\nu_i \quad (6)$$

$$-TS = K_B T \sum_i \ln\left\{1 - e^{\frac{h\nu_i}{K_B T}}\right\} - \sum_i h\nu_i \left\{\frac{1}{e^{\frac{h\nu_i}{K_B T}}}\right\} \quad (7)$$

Where E_{total}, $E_{surface}$, and E_{gas} are the total energies for different adsorption sites, substrate slab, and adsorbent, respectively. The h and ν are the Planck constant and vibrational frequency. There are only adsorbate vibrational modes were calculated explicitly, while the catalyst sheet is fixed. K_B is the Boltzmann constant.

To ensure the accuracy of the calculations, we further performed free energy and density of states (DOS) calculations using the spin-orbit coupling (SOC) method and

the GGA+U method for comparison with the GGA approach. The U_{eff} = 4 eV, 3.3 eV, and 6.4 eV were used to the strongly localized 3d orbitals of Fe, Co, and Ni, respectively. [Chem. Phy., 2021, 545, 111160]. The energy barriers of transition states were calculated by a climbing image nudged elastic band method (CINEB) (Chem. Mater. 2024, 36, 6205-6218).

Supplementary Figures

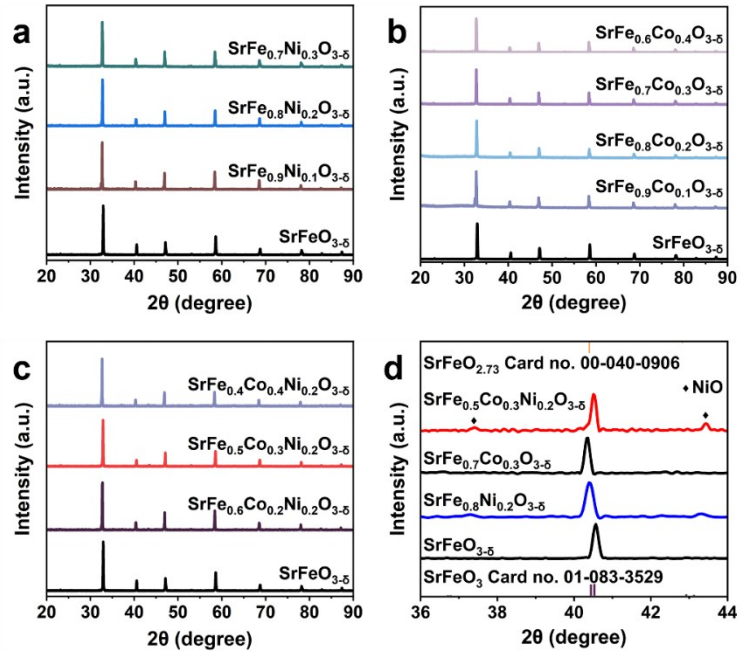

Fig. S1. XRD patterns of (a) $SrFe_{1-x}Ni_xO_{3-\delta}$ (x = 0, 0.1, 0.2, 0.3), (b) $SrFe_{1-y}Co_yO_{3-\delta}$ (y = 0, 0.1, 0.2, 0.3, 0.4), and (c) $SrFe_{0.8-y}Co_yNi_{0.2}O_{3-\delta}$ (y = 0.2, 0.3, 0.4) and $SrFeO_{3-\delta}$. (d) Enlarged XRD patterns of $SrFe_{0.5}Co_{0.3}Ni_{0.2}O_{3-\delta}$, $SrFe_{0.8}Ni_{0.2}O_{3-\delta}$, $SrFe_{0.7}Co_{0.3}O_{3-\delta}$, and $SrFeO_{3-\delta}$.

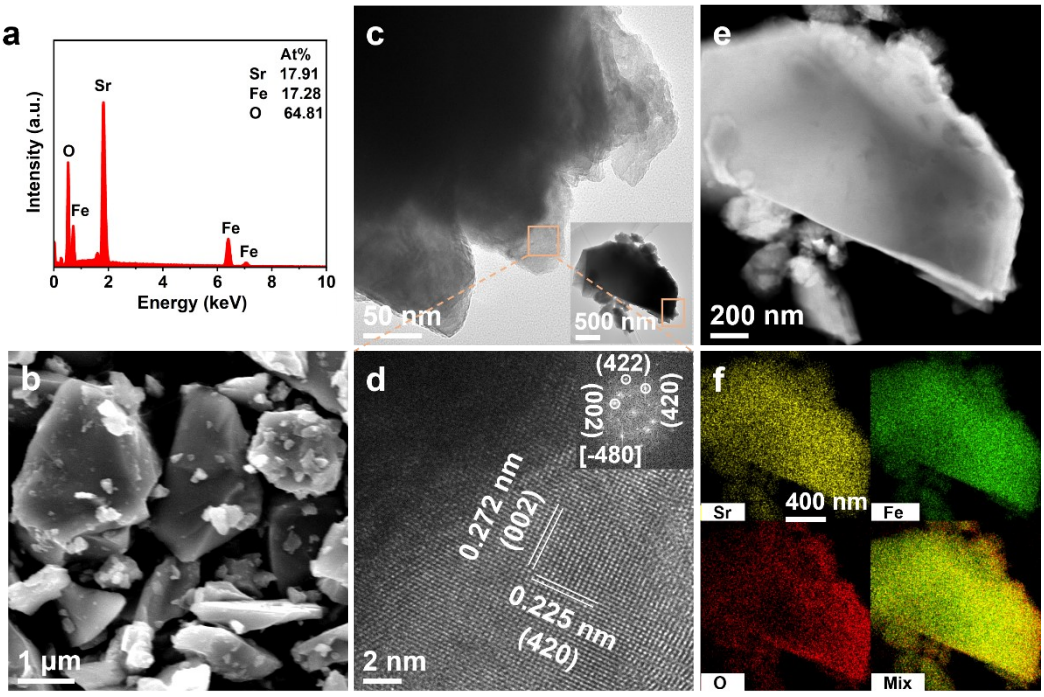

Fig. S2. (a) EDS, (b) SEM image, (c) high-magnification image, (d) HRTEM image, (e) HAADF-STEM image, and (e) the corresponding EDS elemental mapping images of $SrFeO_{3-\delta}$. The inset in c is a low-magnification image of $SrFeO_{3-\delta}$.

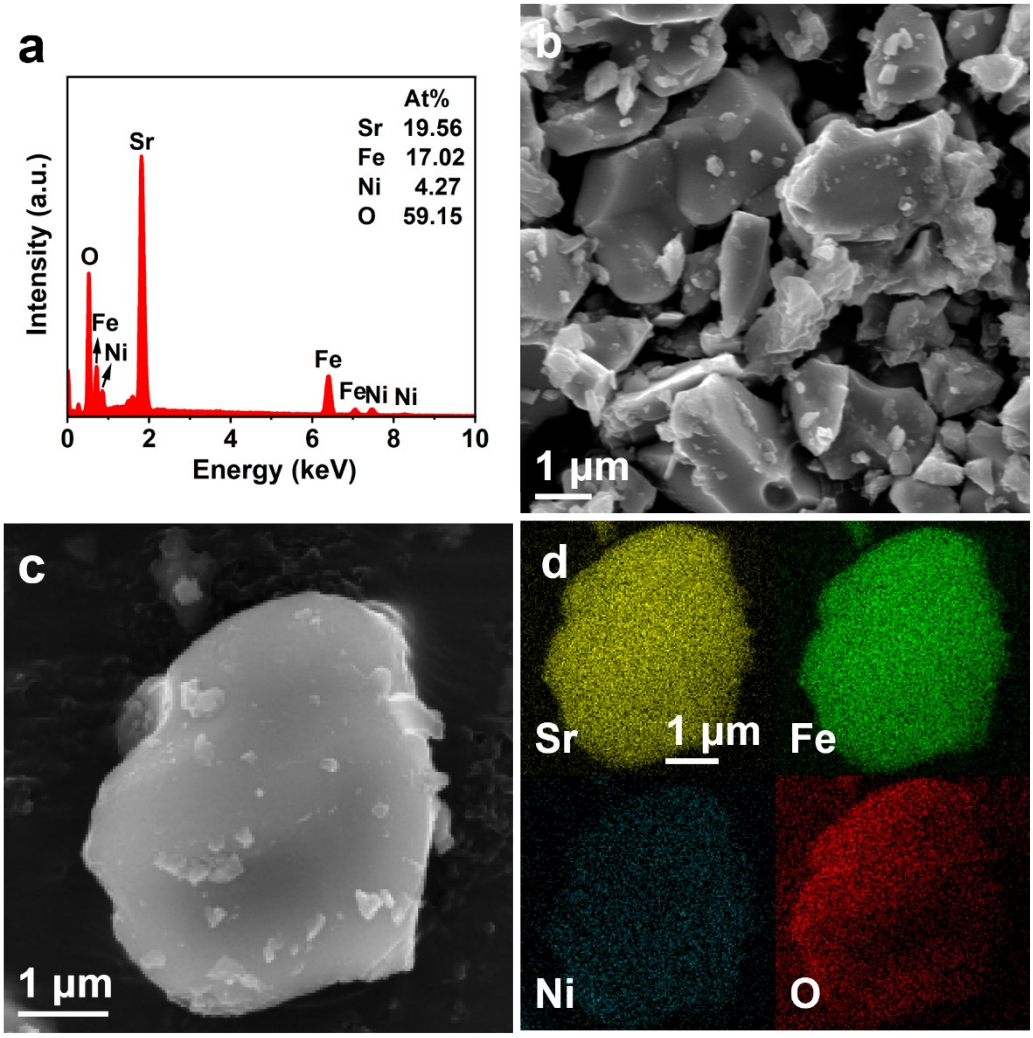

Fig. S3. (a) EDS, (b) SEM image, (c) enlarged SEM image, (d) HAADF-STEM image, and (e) the corresponding EDS elemental mapping images of $SrFe_{0.8}Ni_{0.2}O_{3-\delta}$.

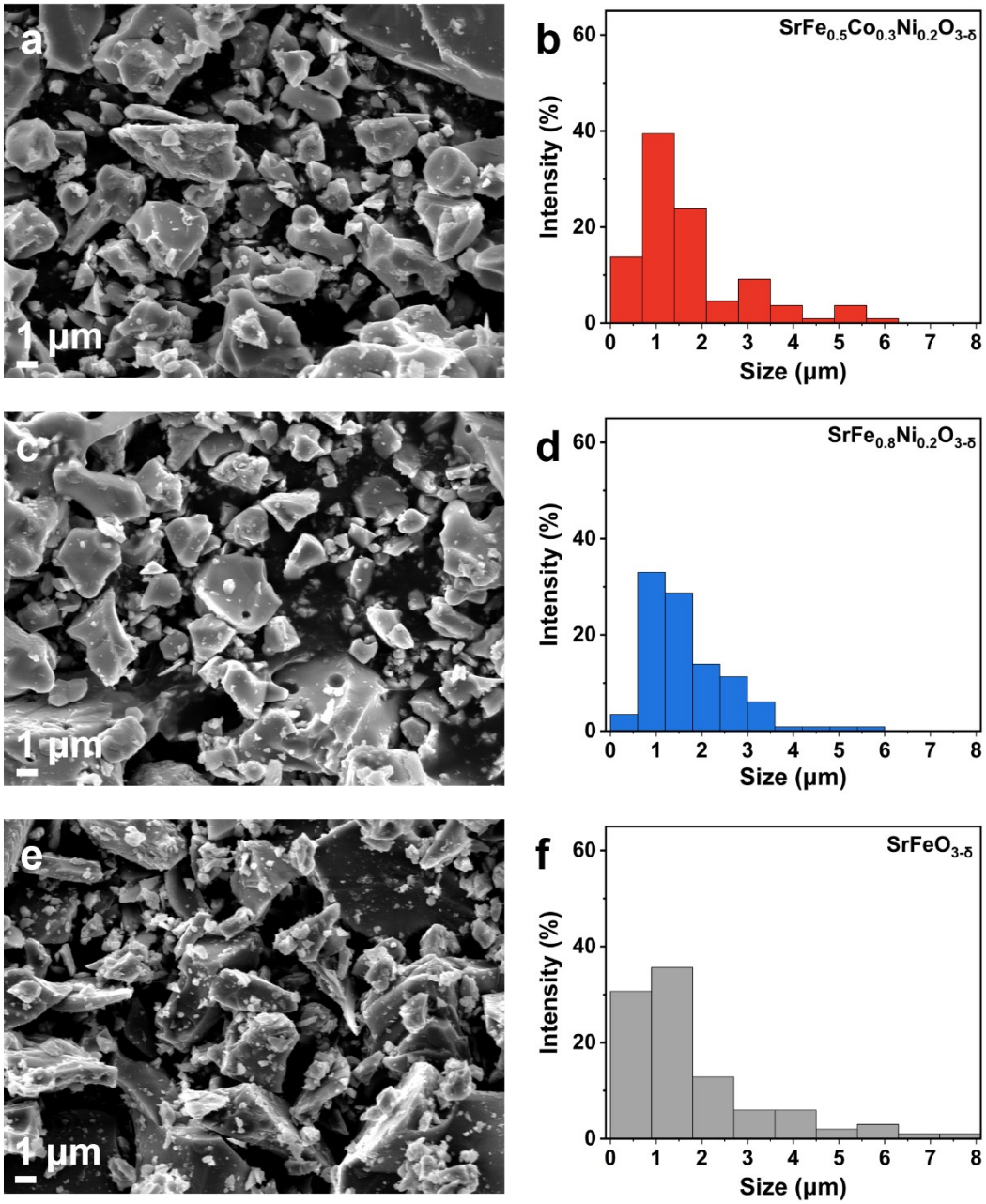

Fig. S4. SEM images and size distributions of (a, b) $SrFe_{0.5}Co_{0.3}Ni_{0.2}O_{3-\delta}$, (c, d) $SrFe_{0.8}Ni_{0.2}O_{3-\delta}$, and (e, f) $SrFeO_{3-\delta}$.

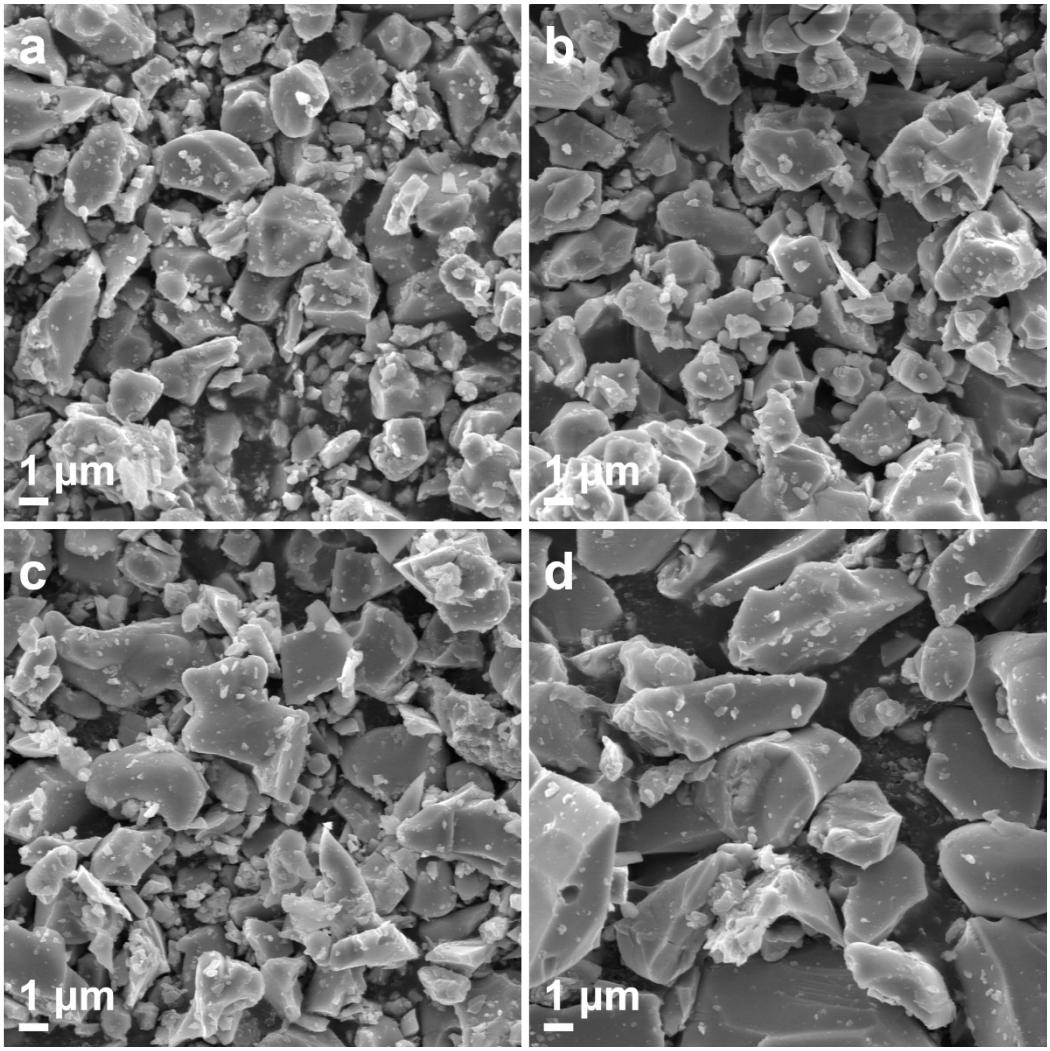

Fig. S5. SEM images of (a) $SrFe_{0.9}Ni_{0.1}O_{3-\delta}$, (b) $SrFe_{0.7}Ni_{0.3}O_{3-\delta}$, (c) $SrFe_{0.6}Co_{0.2}Ni_{0.2}O_{3-\delta}$ and (d) $SrFe_{0.4}$ $Co_{0.4}Ni_{0.2}O_{3-\delta}$.

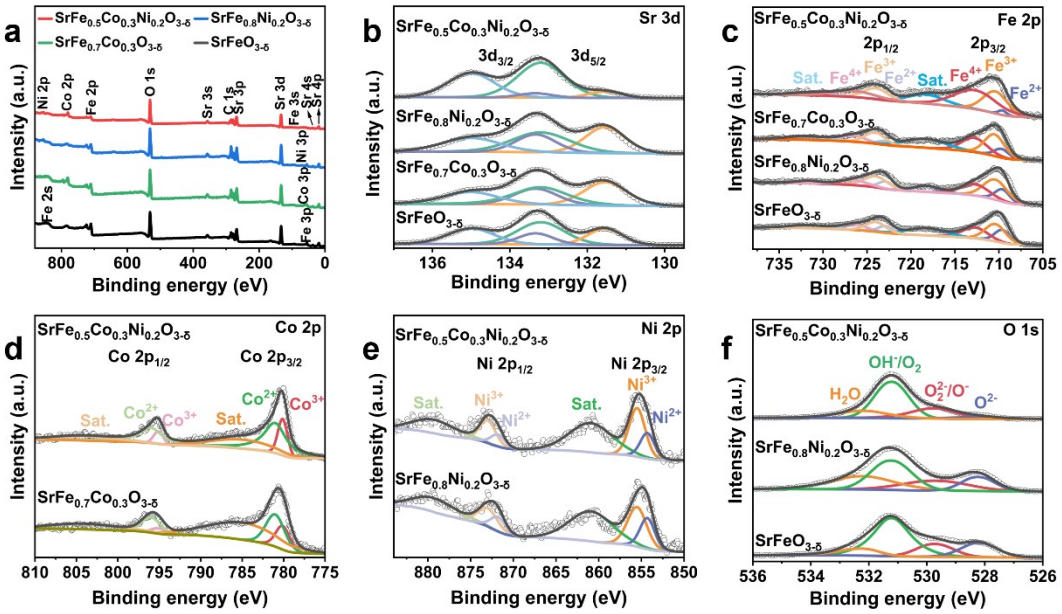

Fig. S6. (a) Survey XPS spectra, high-resolution (b) Sr 3d and (c) Fe 2p XPS spectra of $SrFe_{0.5}Co_{0.3}Ni_{0.2}O_{3-\delta}$, $SrFe_{0.8}Ni_{0.2}O_{3-\delta}$, $SrFe_{0.7}Co_{0.3}O_{3-\delta}$, and $SrFeO_{3-\delta}$. (d) High-resolution Co 2p XPS spectra of $SrFe_{0.5}Co_{0.3}Ni_{0.2}O_{3-\delta}$, and $SrFe_{0.7}Co_{0.3}O_{3-\delta}$. (e) Ni 2p XPS spectra of $SrFe_{0.5}Co_{0.3}Ni_{0.2}O_{3-\delta}$ and $SrFe_{0.8}Ni_{0.2}O_{3-\delta}$. (f) High-resolution O 1s XPS spectra of $SrFe_{0.5}Co_{0.3}Ni_{0.2}O_{3-\delta}$, $SrFe_{0.8}Ni_{0.2}O_{3-\delta}$ and $SrFeO_{3-\delta}$.

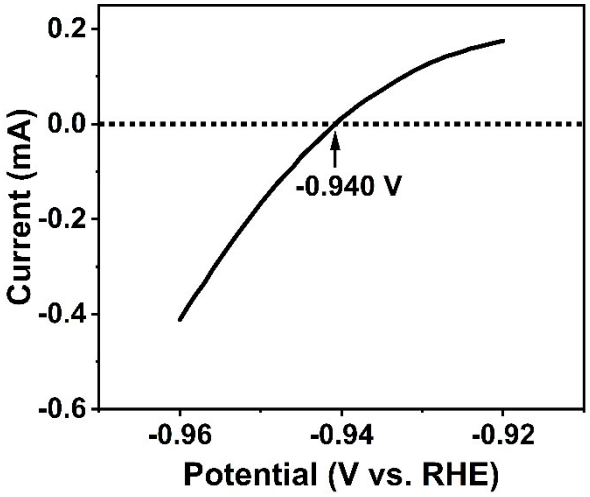

Fig. S7. The current-potential curve for the calibration of the Hg/HgO electrode to RHE in the H_2-saturated 1.0 M KOH aqueous solution by using a Pt plate as the working electrode

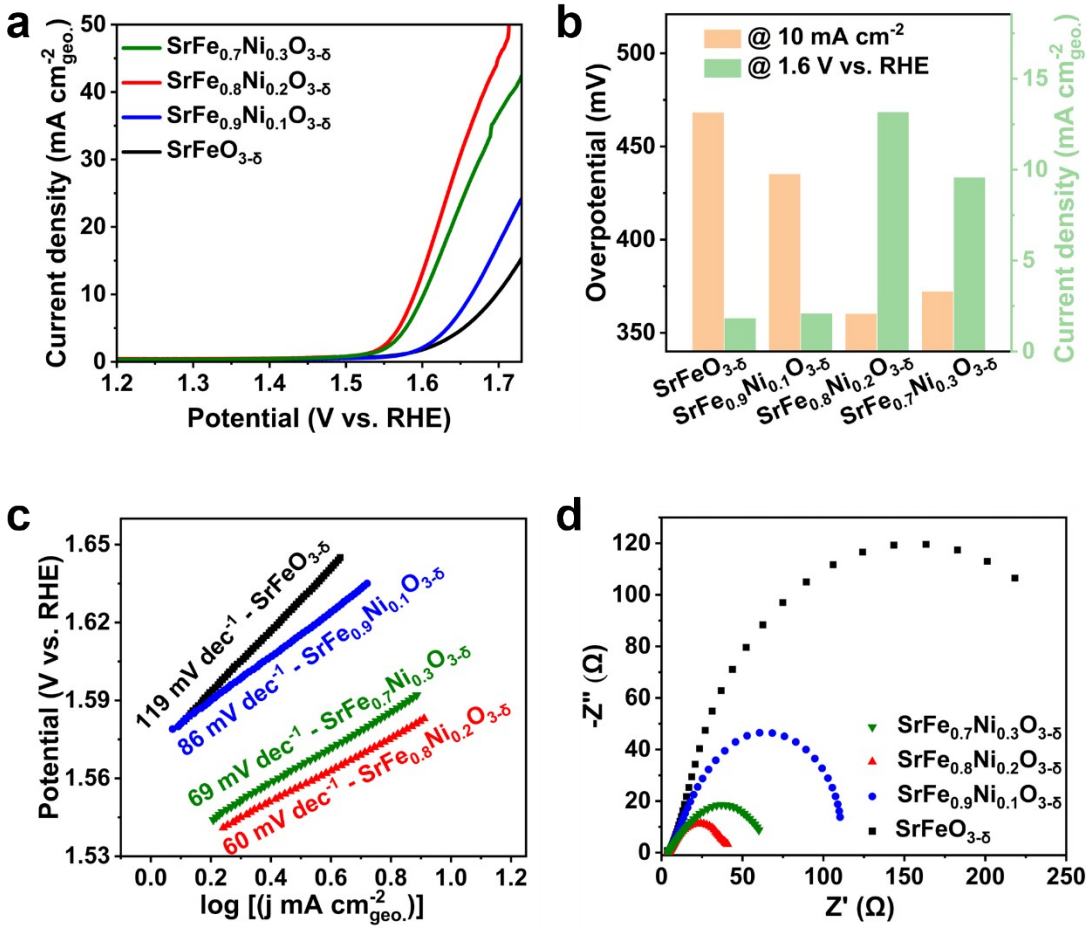

Fig. S8. (a) Polarization curves, overpotentials, and current densities at a potential of 1.6 V (vs. RHE), (c) Tafel slopes, and (d) Nyquist plots of $SrFe_{1-x}Ni_xO_{3-\delta}$ (x = 0, 0.1, 0.2, 0.3).

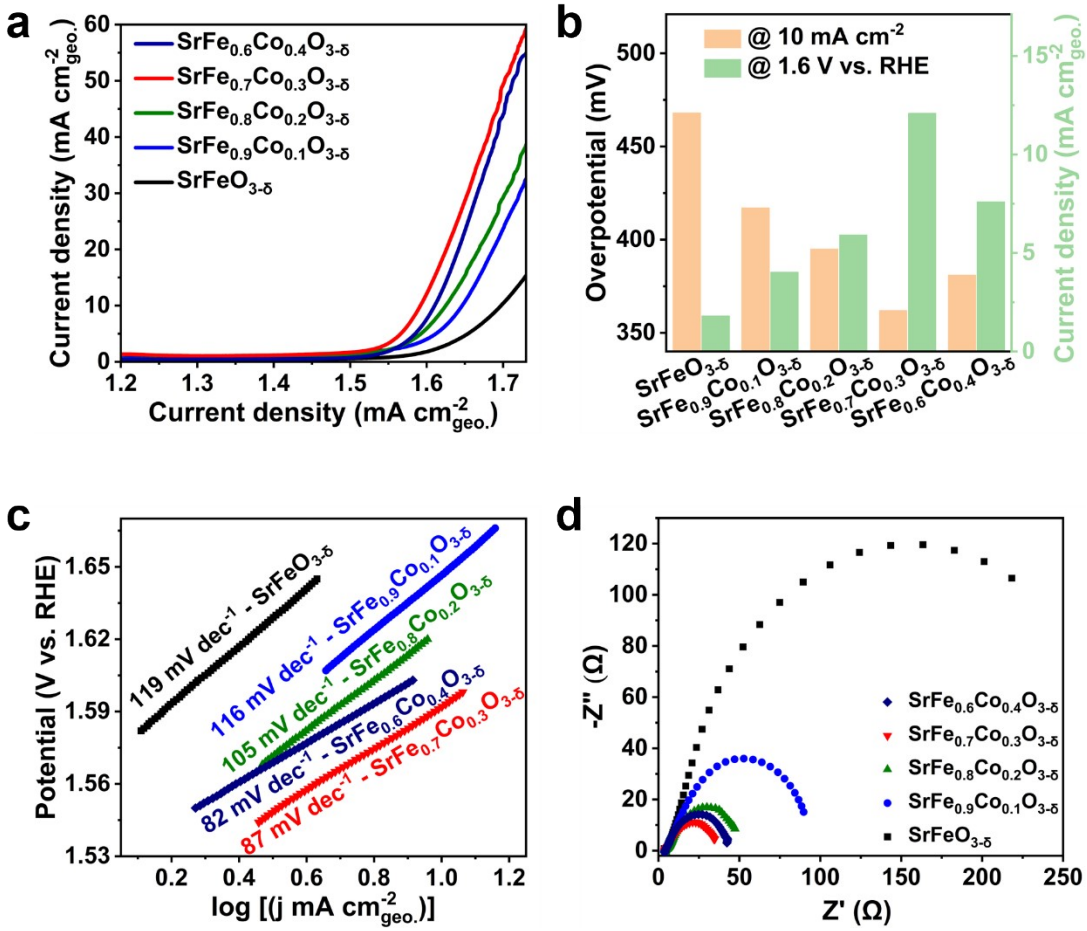

Fig. S9. (a) Polarization curves, overpotentials, and current densities at a potential of 1.6 V (vs. RHE), (c) Tafel slopes, and (d) Nyquist plots of $SrFe_{1-y}Co_yO_{3-\delta}$ (y = 0, 0.1, 0.2, 0.3, 0.4).

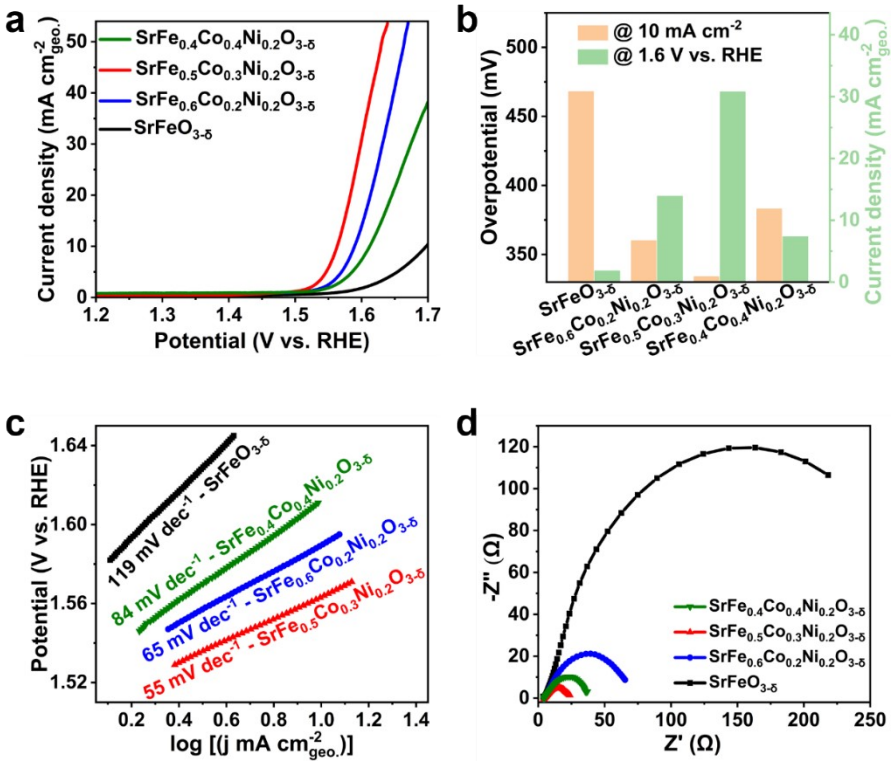

Fig. S10. (a) Polarization curves, (b) histogram of overpotentials and current densities at the potential of 1.6 V (vs. RHE), (c) Tafel slopes, and (d) Nyquist plots of $SrFe_{0.8-y}Co_yNi_{0.2}O_{3-\delta}$ (y = 0.2, 0.3, 0.4) and $SrFeO_{3-\delta}$.

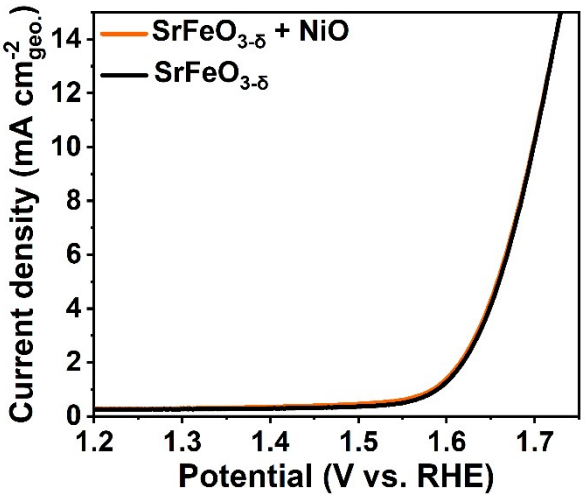

Fig. S11. Polarization curves of $SrFeO_{3-\delta}$, and a mixture of $SrFeO_{3-\delta}$ and NiO.

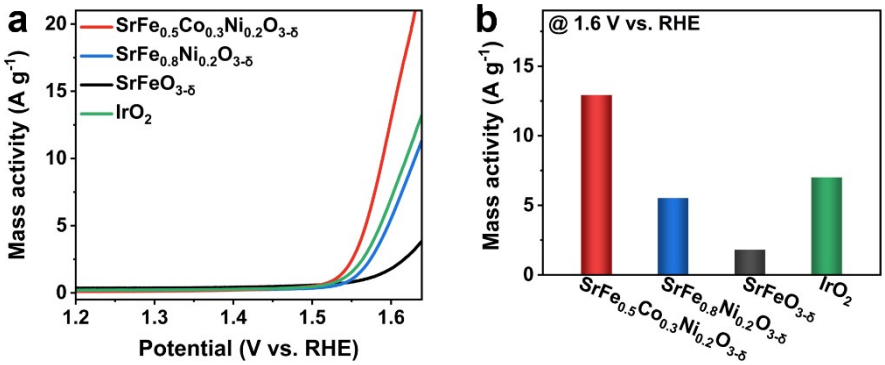

Fig. S12. (a) Mass activities and (b) histogram of mass activities at the potential of 1.6 V (vs. RHE) for $SrFe_{0.5}Co_{0.3}Ni_{0.2}O_{3-\delta}$, $SrFe_{0.8}Ni_{0.2}O_{3-\delta}$, $SrFeO_{3-\delta}$, and IrO_2.

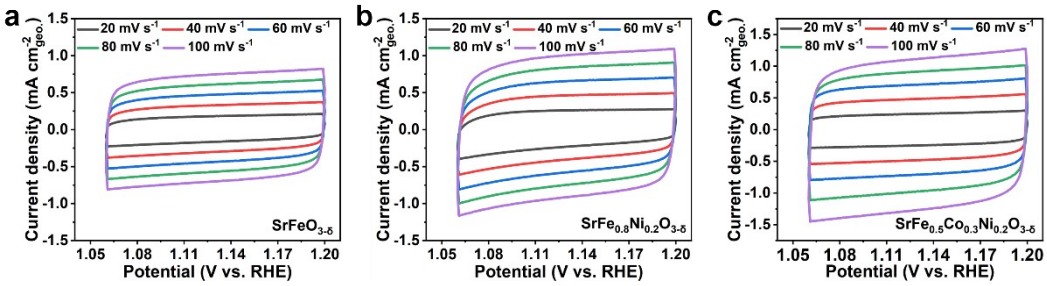

Fig. S13. (a-c) CV curves of $SrFeO_{3-\delta}$, $SrFe_{0.8}Ni_{0.2}O_{3-\delta}$, and $SrFe_{0.5}Co_{0.3}Ni_{0.2}O_{3-\delta}$ at different scan rates. The capacitive currents were measured at 1.14 V vs. RHE.

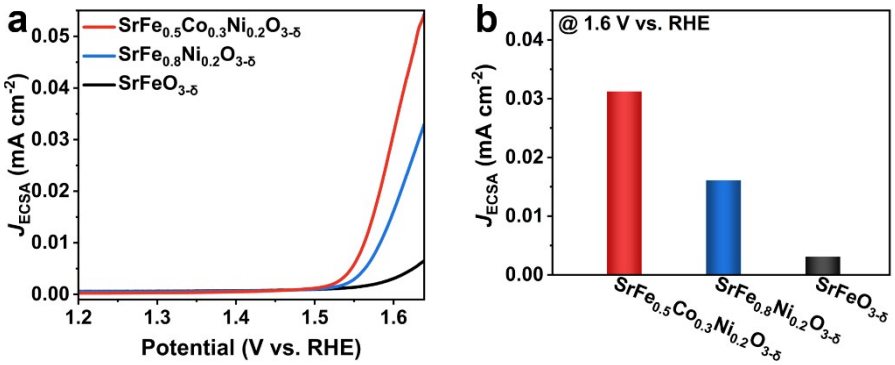

Fig. S14. (a) Specific activities and (b) histogram of specific activities at the potential of 1.6 V (vs. RHE) for $SrFe_{0.5}Co_{0.3}Ni_{0.2}O_{3-\delta}$, $SrFe_{0.8}Ni_{0.2}O_{3-\delta}$, and $SrFeO_{3-\delta}$.

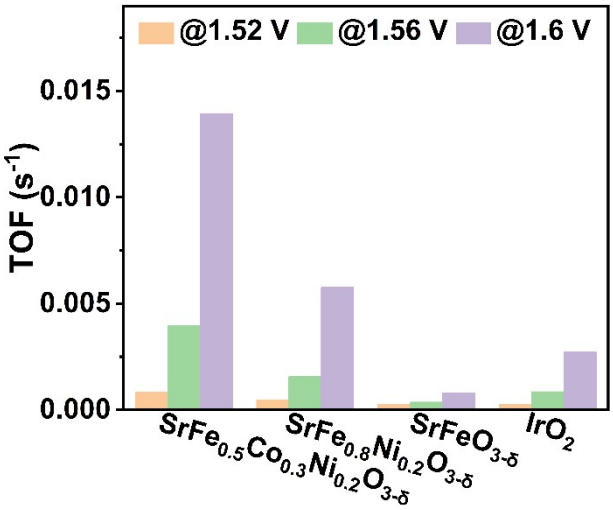

Fig. S15. The turnover frequency (TOF) of $SrFe_{0.5}Co_{0.3}Ni_{0.2}O_{3-\delta}$, $SrFe_{0.8}Ni_{0.2}O_{3-\delta}$, $SrFeO_{3-\delta}$, and IrO_2.

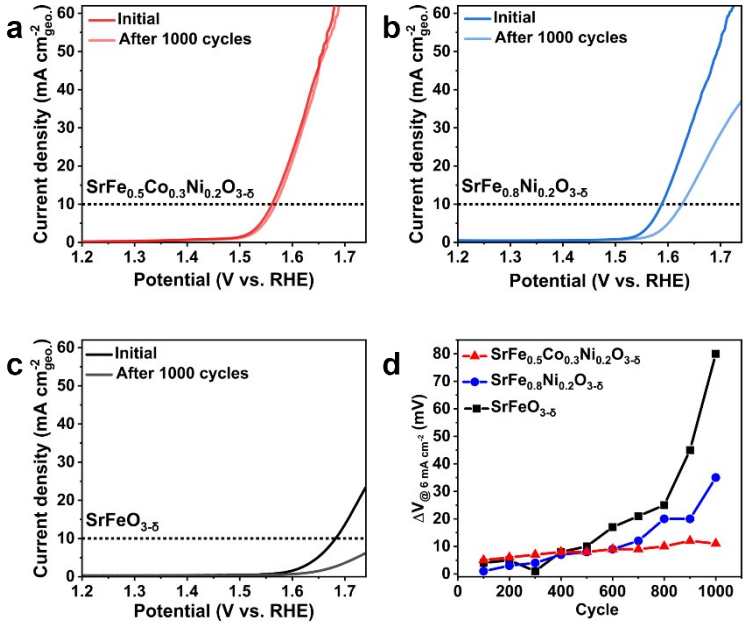

Fig. S16. CV scans for (a) $SrFe_{0.5}Co_{0.3}Ni_{0.2}O_{3-\delta}$, (b) $SrFe_{0.8}Ni_{0.2}O_{3-\delta}$, and (c) $SrFeO_{3-\delta}$ before and after 1000 cycles in 1 M KOH solutions. (d) Potential difference (ΔV) at a current density of 6 mA cm^{-2} for $SrFe_{0.5}Co_{0.3}Ni_{0.2}O_{3-\delta}$, $SrFe_{0.8}Ni_{0.2}O_{3-\delta}$ and $SrFeO_{3-\delta}$ over 1000 cycles.

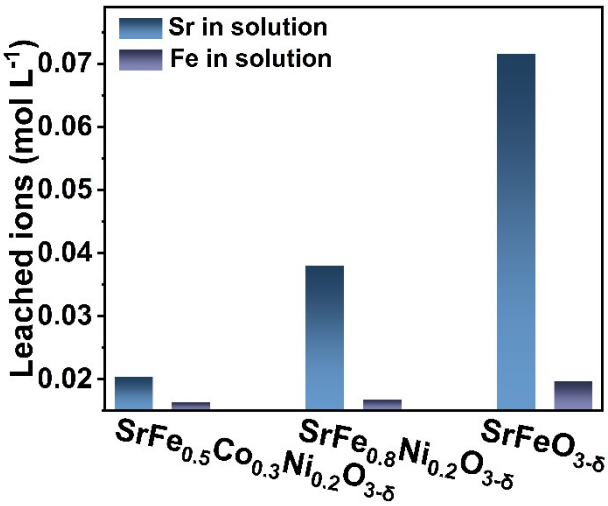

Fig. S17. The amount of Sr and Fe ions of $SrFe_{0.5}Co_{0.3}Ni_{0.2}O_{3-\delta}$, $SrFe_{0.8}Ni_{0.2}O_{3-\delta}$, $SrFeO_{3-\delta}$ dissolved in the electrolyte after durable test.

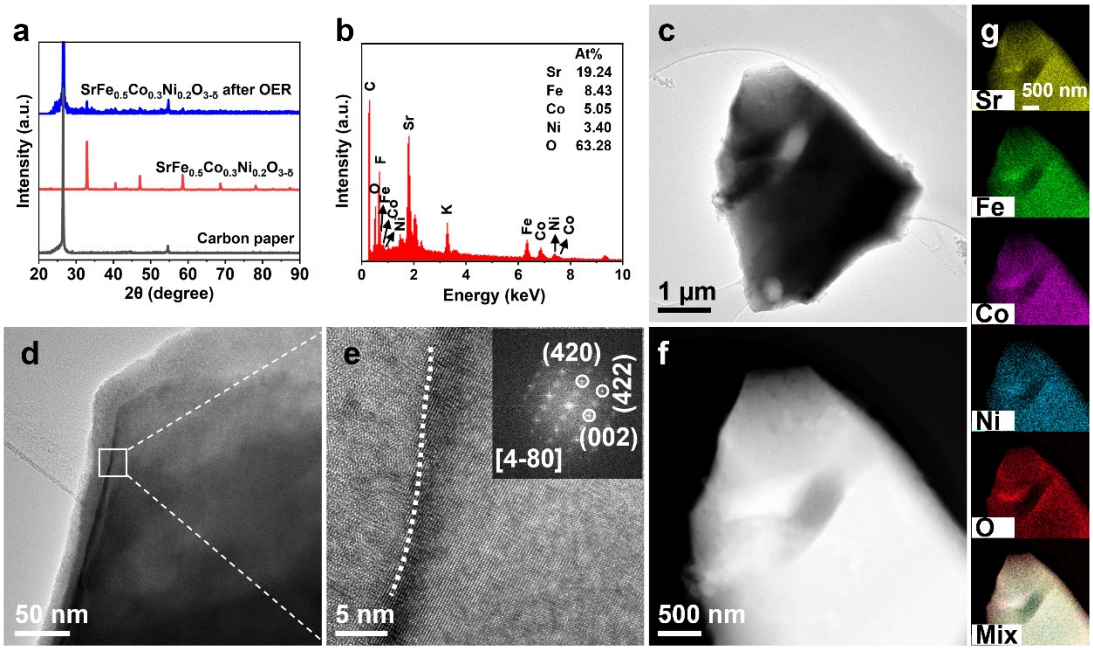

Fig. S18. (a) XRD patterns of carbon paper, $SrFe_{0.5}Co_{0.3}Ni_{0.2}O_{3-\delta}$ before and after OER. (b) EDS of $SrFe_{0.5}Co_{0.3}Ni_{0.2}O_{3-\delta}$ after OER. (c) Low-magnification TEM image, (d) high-magnification TEM image, (e) HRTEM image, (f) HADDF-STEM image, and (g) the corresponding elemental mapping images of a particle for $SrFe_{0.5}Co_{0.3}Ni_{0.2}O_{3-\delta}$ after OER.

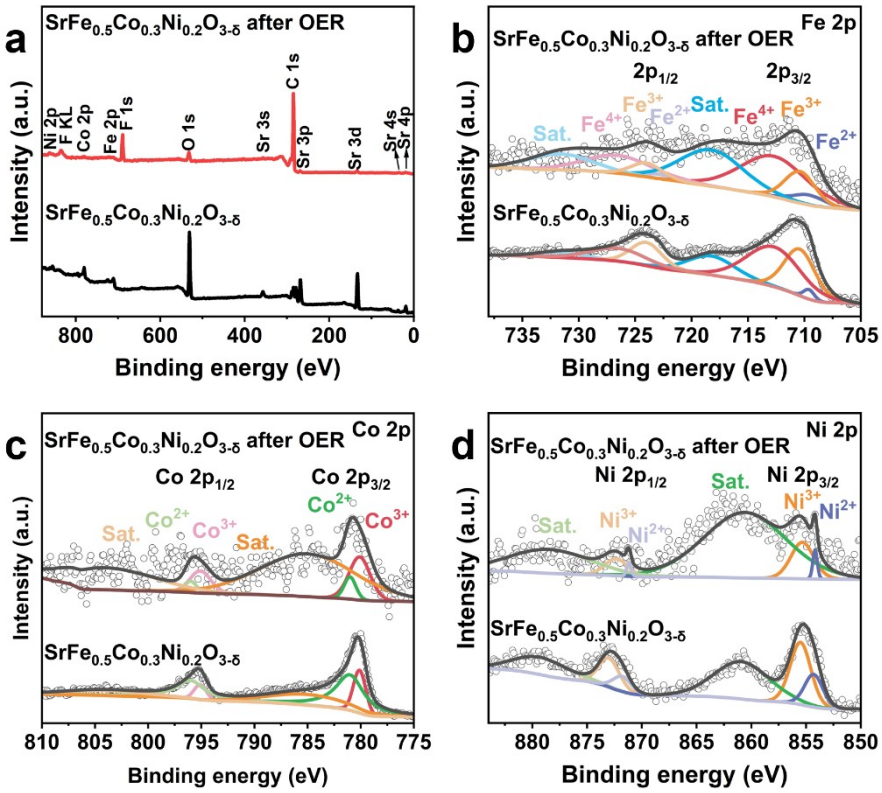

Fig. S19. (a) Survey XPS spectra, high-resolution (b) Fe 2p, (c) Co 2p, (d) Ni 2p XPS spectra of $SrFe_{0.5}Co_{0.3}Ni_{0.2}O_{3-\delta}$ before and after OER.

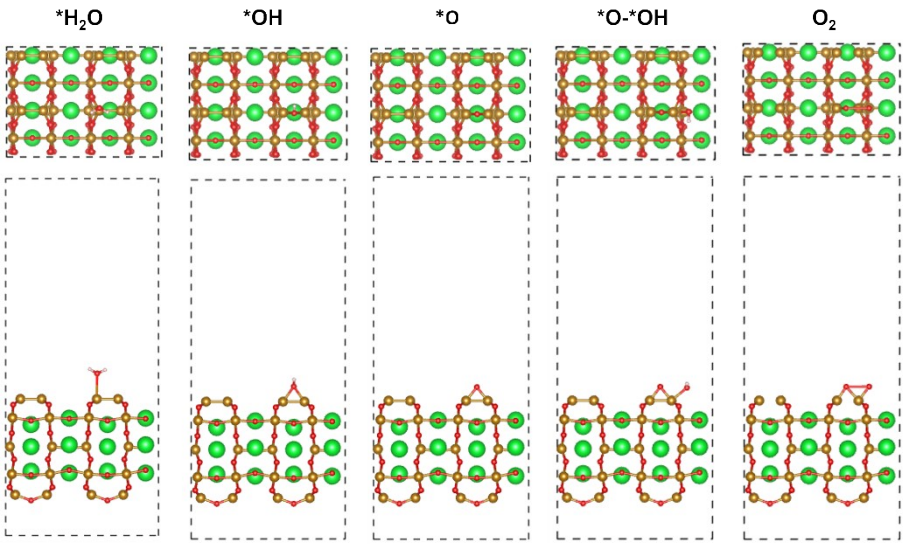

Fig. S20. Schematic diagram of structures of adsorbates on $SrFeO_3$.

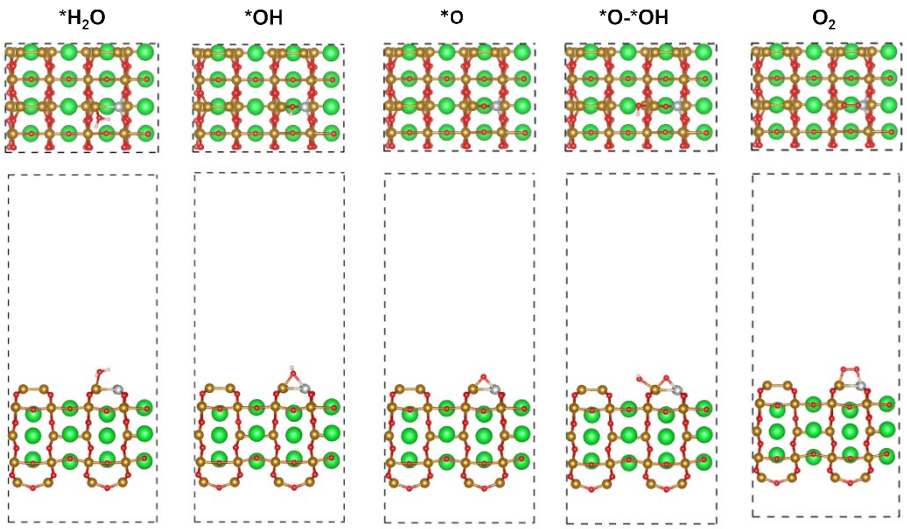

Fig. S21. Schematic diagram of structures of adsorbates on Ni-doped $SrFeO_3$.

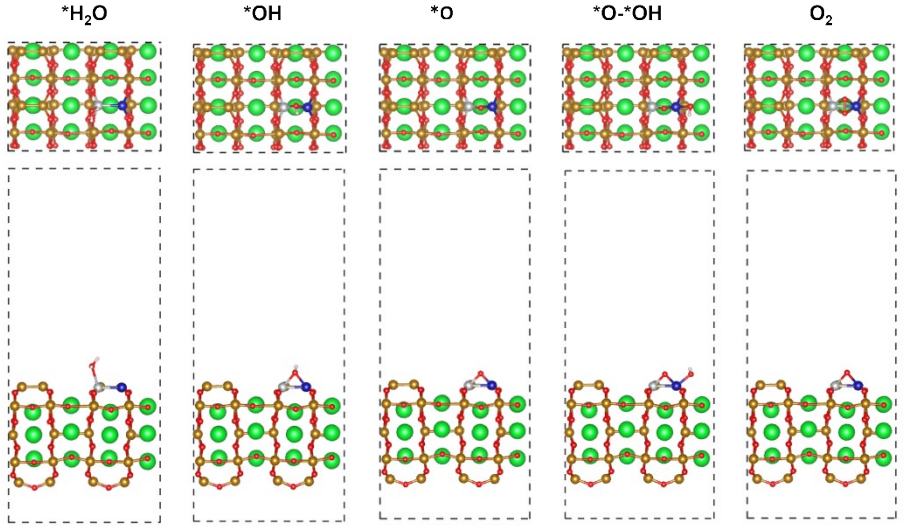

Fig. S22. Schematic diagram of structures of adsorbates on Co and Ni codoped $SrFeO_3$.

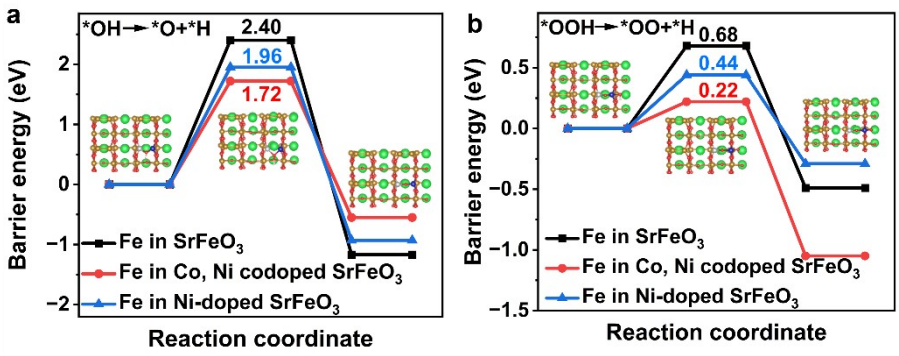

Fig. S23. Reaction barrier energy of (a) *OH→*O+*H (b) *OOH→*OO+*H calculated by using the CINEB method for $SrFeO_3$, Ni-doped $SrFeO_3$, and Co, Ni codoped $SrFeO_3$.

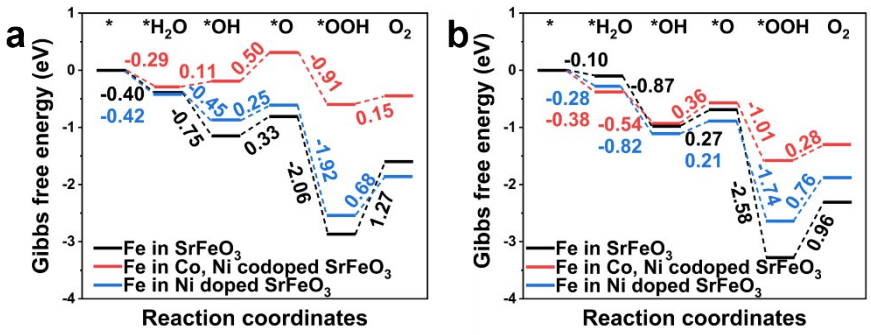

Fig. S24. Gibbs free energy diagram of Fe sites in $SrFeO_3$, Ni-doped of $SrFeO_3$, and Co and Ni codoped of $SrFeO_3$ calculated by (a) SOC and (b) GGA+U method.

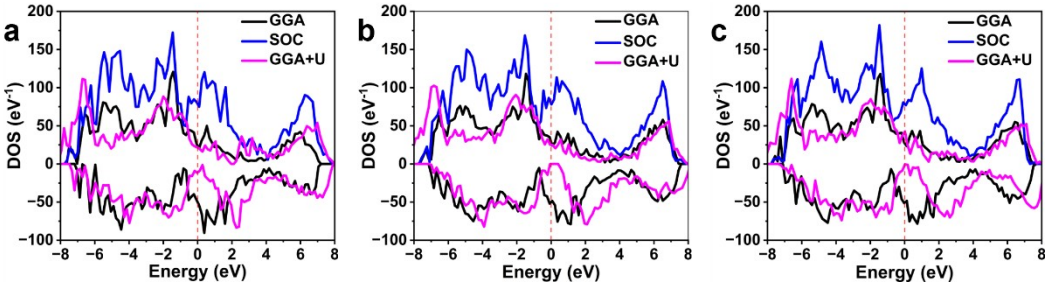

Fig. S25. DOS of (a) $SrFeO_3$, (b) Ni-doped $SrFeO_3$, and Co, Ni codoped $SrFeO_3$ calculated by GGA, SOC, and GGA+U method.

Table S1. ICP-MS results of $SrFe_{0.5}Co_{0.3}Ni_{0.2}O_{3-\delta}$, $SrFe_{0.8}Ni_{0.2}O_{3-\delta}$, and $SrFeO_{3-\delta}$ before OER.

Simple	Sr (10^{-6} mol)	Fe (10^{-6} mol)	Co (10^{-6} mol)	Ni (10^{-6} mol)
$SrFe_{0.5}Co_{0.3}Ni_{0.2}O_{3-\delta}$	6.587	3.389	2.015	1.339
$SrFe_{0.8}Ni_{0.2}O_{3-\delta}$	7.059	5.752		1.320
$SrFeO_{3-\delta}$	48.348	49.717		

Table S2. The relative ratio of fitted Fe species in $SrFe_{0.5}Co_{0.3}Ni_{0.2}O_{3-\delta}$, $SrFe_{0.8}Ni_{0.2}O_{3-\delta}$, and $SrFeO_{3-\delta}$.

Samples	Fe^{2+}(%)	Fe^{3+}(%)	Fe^{4+} (%)	Sat.
$SrFe_{0.5}Co_{0.3}Ni_{0.2}O_{3-\delta}$	2.36	34.15	45.52	17.97
$SrFe_{0.8}Ni_{0.2}O_{3-\delta}$	17.47	43.22	26.26	13.05
$SrFeO_{3-\delta}$	18.21	33.37	24.82	23.60

Table S3. The relative ratio of fitted Ni species in $SrFe_{0.5}Co_{0.3}Ni_{0.2}O_{3-\delta}$, and $SrFe_{0.8}Ni_{0.2}O_{3-\delta}$.

Samples	Ni^{2+}	Ni^{3+}	Sat.
$SrFe_{0.5}Co_{0.3}Ni_{0.2}O_{3-\delta}$	18.48	30.54	50.98
$SrFe_{0.8}Ni_{0.2}O_{3-\delta}$	15.19	32.80	52.01

Table S4. The relative ratio of fitted oxygen species in $SrFe_{0.5}Co_{0.3}Ni_{0.2}O_{3-\delta}$, $SrFe_{0.8}Ni_{0.2}O_{3-\delta}$, and $SrFeO_{3-\delta}$.

Samples	O^{2-} (%)	O_2^{2-}/O^- (%)	OH^-/O_2 (%)	H_2O (%)
$SrFe_{0.5}Co_{0.3}Ni_{0.2}O_{3-\delta}$	5.26	22.40	54.01	18.33
$SrFe_{0.8}Ni_{0.2}O_{3-\delta}$	14.64	20.50	36.87	27.99
$SrFeO_{3-\delta}$	18.41	16.54	53.21	11.84

Table S5. Comparison of OER activities of perovskite oxides.

Catalyst	Electrolyte	Overpotential @ 10 mA cm^{-2} (mV)	Tafel slope (mV dec^{-1})	Ref.
$SrFe_{0.5}Co_{0.3}Ni_{0.2}O_{3-\delta}$	**1 M KOH**	**334**	**55**	**This work**
$La_{0.5}Sr_{0.5}CoO_{3-\delta}$&$MoSe_2$	1 M KOH	360	77	8
$La_{0.5}Ba_{0.25}Sr_{0.25}CoO_{2.9-\delta}F_{0.1}$	1 M KOH	390	113	9
$PrBa_{0.5}Sr_{0.5}Co_{1.5}Fe_{0.5}O_{5+\delta}$ NT-V-20 min	1 M KOH	319	60	10
$PrBa_{0.5}Sr_{0.5}Co_{1.5}Fe_{0.5}O_{5+\delta}$ NT80-V-20 min	1 M KOH	313	80	10
$La_{0.7}Sr_{0.3}Co_{0.25}Mn_{0.75}O_3$-NPs-800	1 M KOH	340	111	11
$LaNi_{0.8}Fe_{0.2}O_{3-\delta}$-NR	1 M KOH	302	50	12
$PrBaCo_2O_{5.75}$	1 M KOH	360	70	13
$La_{0.5}(Ba_{0.4}Sr_{0.4}Ca_{0.2})_{0.5}Co_{0.8}Fe_{0.2}O_3$	1 M KOH	350	96	14
$La_{0.5}(Ba_{0.4}Sr_{0.4}Ca_{0.2})_{0.5}Co_{0.8}Fe_{0.2}O_3$/rGO	1 M KOH	338	80	14
$SrNb_{0.1}Co_{0.7}Fe_{0.2}O_{3-\delta}$	1 M KOH	370	48	15
$NdBaMn_2O_{5.5}$	1 M KOH	370	75	16
La_2NiMnO_6	1 M KOH	370	58	17
$(PrBa_{0.8}Ca_{0.2})_{0.95}(Co_{1.5}Fe_{0.5})_{0.95}Co_{0.05}O_{5+\delta}$	1 M KOH	380	99	18
$Sr_{0.95}Ce_{0.05}Fe_{0.9}Ni_{0.1}O_{3-\delta}$	1 M KOH	340	51	19
$Sr(Co_{0.8}Fe_{0.2})_{0.7}B_{0.3}O_{3-\delta}$	1 M KOH	240	58	20

$La_{0.5}Sr_{1.5}Ni_{0.7}Fe_{0.3}O_{4+\delta}$	0.1 M KOH	360	44	21
Si-SCO	0.1 M KOH	417	66	22
$Ba_4Sr_4(Co_{0.8}Fe_{0.2})_4O_{15}$	0.1 M KOH	340	47	23

Table S6. Gibbs free energy of each step for $SrFeO_3$, Ni-doped $SrFeO_3$, and Co, Ni codoped $SrFeO_3$.

Sample	Gibbs free energy (eV)					
	*	*H_2O	*OH	*O	*OOH	*OO
$SrFeO_3$	0	-0.05	-0.77	-0.28	-1.92	0.95
Ni-doped $SrFeO_3$	0	-0.35	-0.25	0.2	-2.49	0.71
Co, Ni codoped $SrFeO_3$	0	-0.17	-0.05	0.4	-1.26	0.29

Reference

(1) G. Kresse and J. Furthmüller, *Phys. Rev. B*, 1996, **54**, 11169.

(2) J. P. Perdew, K. Burke and M. Ernzerhof, *Phys. Rev. Lett.*, 1996, **77**, 3865.

(3) G. Kresse and D. Joubert, *Phys. Rev. B*, 1999, **59**, 1758.

(4) S. Grimme, *J. Comput. Chem.*, 2006, **27**, 1787.

(5) L. Seixas, A. Carvalho and A. H. Castro Neto, *Phys. Rev. B*, 2015, **91**, 155138.

(6) M. Wang, L. Li, G. Zhao, Z. Xu, S. Hussain, M. Wang, G. Qiao and G. Liu, *Appl. Surf. Sci.*, 2020, **504**, 144374.

(7) H. Yang, Y. Wu, G. Li, Q. Lin, Q. Hu, Q. Zhang, J. Liu and C. He, *J. Am. Chem. Soc.*, 2019,

141, 12717.

(8) N. K. Oh, C. Kim, J. Lee, O. Kwon, Y. Choi, G. Y. Jung, H. Y. Lim, S. K. Kwak, G. Kim and H. Park, *Nat. Commun.*, 2019, **10**, 1723.

(9) B. Hua, M. Li, W. Pang, W. Tang, S. Zhao, Z. Jin, Y. Zeng, B. Shalchi Amirkhiz and J.-L. Luo, *Chem*, 2018, **4**, 2902.

(10) Y. Zhu, L. Zhang, B. Zhao, H. Chen, X. Liu, R. Zhao, X. Wang, J. Liu, Y. Chen and M. Liu, *Adv. Funct. Mater.*, 2019, **29**, 1901783.

(11) X. Yu, M. Wang, X. Gong, Z. Guo, Z. Wang and S. Jiao, *Adv. Energy Mater.*, 2018, **8**, 1802445.

(12) H. Wang, J. Wang, Y. Pi, Q. Shao, Y. Tan and X. Huang, *Angew. Chem. Int. Ed.*, 2019, **58**, 2316.

(13) X. Miao, L. Wu, Y. Lin, X. Yuan, J. Zhao, W. Yan, S. Zhou and L. Shi, *Chem. Commun.*, 2019, **55**, 1442.

(14) B. Hua, M. Li, Y.-Q. Zhang, Y.-F. Sun and J.-L. Luo, *Adv. Energy Mater.*, 2017, **7**, 1700666.

(15) Y. Zhu, W. Zhou, Y. Zhong, Y. Bu, X. Chen, Q. Zhong, M. Liu and Z. Shao, *Adv. Energy Mater.*, 2017, **7**, 1602122.

(16) C. Chen, Z. Wang, B. Zhang, L. Miao, J. Cai, L. Peng, Y. Huang, J. Jiang, Y. Huang, L. Zhang and J. Xie, *Energy Storage Mater.*, 2017, **8**, 161.

(17) Y. Tong, J. Wu, P. Chen, H. Liu, W. Chu, C. Wu and Y. Xie, *J. Am. Chem. Soc.*, 2018, **140**, 11165.

(18) B. Hua, M. Li, Y.-F. Sun, Y.-Q. Zhang, N. Yan, J. Chen, T. Thundat, J. Li and J.-L. Luo, *Nano Energy*, 2017, **32**, 247.

(19) S. She, Y. Zhu, X. Wu, Z. Hu, A. Shelke, W.-F. Pong, Y. Chen, Y. Song, M. Liang, C.-T.

Chen, H. Wang, W. Zhou and Z. Shao, *Adv. Funct. Mater.*, 2022, **32**, 2111091.

(20) S. She, Y. Zhu, Y. Chen, Q. Lu, W. Zhou and Z. Shao, *Adv. Energy Mater.*, 2019, **9**, 1900429.

(21) R. P. Forslund, W. G. Hardin, X. Rong, A. M. Abakumov, D. Filimonov, C. T. Alexander, J. T. Mefford, H. Iyer, A. M. Kolpak, K. P. Johnston and K. J. Stevenson, *Nat. Commun.*, 2018, **9**, 3150.

(22) Y. Pan, X. Xu, Y. Zhong, L. Ge, Y. Chen, J.-P. M. Veder, D. Guan, R. O'Hayre, M. Li, G. Wang, H. Wang, W. Zhou and Z. Shao, *Nat. Commun*., 2020, **11**, 2002.

(23) Y. Zhu, H. A. Tahini, Z. Hu, Z.-G. Chen, W. Zhou, A. C. Komarek, Q. Lin, H.-J. Lin, C.-T. Chen, Y. Zhong, M. T. Fernández-Díaz, S. C. Smith, H. Wang, M. Liu and Z. Shao, *Adv. Mater.*, 2020, **32**, 1905025.